Functional Modeling of Symmetrical Multipulse Autotransformer Rectifier Units for Aerospace Applications

Tao Yang, Serhiyi Bozhko, *Member, IEEE*, and Greg Asher, *Fellow, IEEE*

***Abstract*—This paper aims to develop a functional model of symmetrical multipulse autotransformer rectifier units (ATRUs) for more-electric aircraft (MEA) applications. The ATRU is seen as the most reliable way readily to be applied in the MEA. Interestingly, there is no model of ATRUs suitable for unbalanced or faulty conditions at the moment. This paper is aimed to fill this gap and develop functional models suitable for both balanced and unbalanced conditions. Using the fact that the dc voltage and current are strongly related to the voltage and current vectors at the ac terminals of ATRUs, a functional model has been developed for the asymmetric ATRUs. The developed functional models are validated through simulation and experiment. The efficiency of the developed model is also demonstrated by comparing with corresponding detailed switching models. The developed functional model shows significant improvement of simulation efficiency, especially under balanced conditions.**

***Index Terms*—Fault conditions, functional modeling, more-electric aircraft (MEA), multipulse rectifier, transformer rectifier unit (TRU).**

I. Introduction

THE more-electric aircraft (MEA) is the developing trend for the next generation of aeroplanes. Recent advances in power electronics, electrical drives, and modern control techniques make it possible to replace many functions that are conventionally managed by hydraulic, pneumatic, and mechanical power, with electrical power driven devices [1]. Such replacement would increase reliability, capability, maintainability, reduced weight and volume, and provide higher survivability in aircraft operations [2]. The passenger aircraft has long been using transformer rectifier unit (TRU) to produce 28 Vdc from 400-Hz ac sources. The use of MEA technology will result in a large number of ac/dc converters supplying power for functions as fuel pumps, cabin pressurization, air conditioning, engine start, and flight control [3]. There are two alternative ways to convert ac power to dc power: the pulse width modulation active front ends, and passive multipulse converters [4]. The former approach seemingly needs considerable development to meet the reliability requirement for aircraft applications. The latter on the contrary may be readily implemented due to its simplicity, high reliability, low cost, and relatively high efficiency [5]. Moreover, there is no need for isolation makes the autotransformers a preferred choice due to their advantage of reduced kilovoltampere ratings and lower cost, smaller size, and weight [6].

Due to the high requirements for input harmonics and output voltage ripple for the ac/dc converter, the 18-pulse autotransformer rectifier unit (ATRU) seems to be a natural choice for aircraft applications. Moreover, some power quality specifications demand that the distortion of the input line current should be typical of an 18-pulse converter system for loads above 5 kW [7]. There are three main types of 18-pulse ATRU topologies: paralleled ATRUs (P-ATRU) [4], direct symmetric ATRUs (DS-ATRU) [5] and direct asymmetric ATRUs (DA-ATRU) [8]. P-ATRU requires an interphase transformer (IPR) for isolation, which increases the overall size of the converter. In addition, design of an IPR is not an easy work. For this reason, the DS-ATRU and DA-ATRU are the two preferred options for aerospace applications.

The ATRU supplies power to the main dc bus and is a critical element in an MEA electrical distribution system. The development of fast simulation models for this device becomes essentially important when developing new architectures of the electrical power system (EPS) for MEA. The possible architectures of the EPS for MEA include various topologies such as variable ac and dc, hybrid ac and dc distributions [9]. To finalize the design of the EPS requires extensive simulation studies, under balanced and unbalanced conditions, in order to assess the system availability, power quality, and transient behavior, etc. Due to the switching behavior of power electronic devices, it is very time consuming, difficult to converge, sometimes even impractical, to simulate such complex EPS with nonlinear, time-varying detailed switching models. Thus, a fast modeling technique is very necessary for system level studies.

Development of models for EPS can be categorized into four modeling levels, as shown in Fig. 1, i.e., from the bottom to the top, component, behavioral, functional, and architectural levels [10]. Component models cover high frequencies, electromagnetic field, and electromagnetic compatibility behavior, and perhaps thermal and mechanical stressing. The modeling bandwidth of component models can be up to in megahertz region if required. Models in behavioral level cover the converter switching behavior and the impact of harmonics. The modeling

Manuscript received May 15, 2014; revised August 6, 2014; accepted October 13, 2014. Date of publication October 23, 2014; date of current version April 15, 2015. This work was supported by the Clean Sky JTI—Systems for green Operations ITD. Recommended for publication by Associate Editor J. Liu.

T. Yang and S. Bozhko are with the Institute of Aerospace Technology, The University of Nottingham, Nottingham NG7 2TU, U.K. (e-mail: tao.yang@nottingham.ac.uk; serhiy.bozhko@nottingham.ac.uk).

G. Asher is with the Department of Electrical and Electronic Engineering, University of Nottingham, Nottingham NG7 2RD, U.K. (e-mail: greg.asher@nottingham.ac.uk).

Color versions of one or more of the figures in this paper are available online at http://ieeexplore.ieee.org.

Digital Object Identifier 10.1109/TPEL.2014.2364682

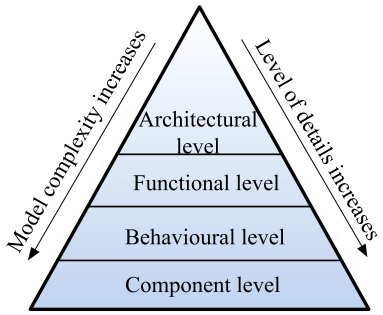

Fig. 1. Multilevel modeling paradigm [10].

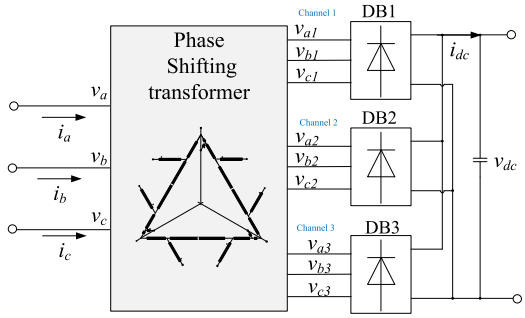

Fig. 2. Configuration of an 18-pulse ATRU.

frequencies can be up to hundreds of kilohertz. The functional level is aimed at addressing low-frequency transient behavior, where the model is able to handle dynamic frequencies up to one-third of the base grid frequency (i.e., 100–150 Hz) with a time waveform accuracy of 95% in respect of the behavioral model. The architectural models are the simpler ones and are representative only of steady-state power consumptions.

This paper aims to develop a fast simulation model of the ATRU at the functional level, where the higher switching harmonics are neglected. The developed functional model provides a solid basis for studying transient response to loading and start-up, stabilities, fault-condition analysis, and overall EPS system performance in MEA. Recently, there are publications of modeling of multipulse rectifiers, including 12-pulse [11], [12] and 18-pulse ATRUs [13], [14]. However, all these models are only suitable for balanced conditions. Small-signal model is proposed in [15] and input impedance model is introduced in [16]. Though useful for assessing the stability margin of the power system, these two models are not applicable for general simulation study of the aircraft EPS.

The developed model is a generalized average model, which is based on the vector concept and is in the *dq* frame. This method has been widely used in modeling electrical machines [10], [17], [18]. This paper will extend this technique in modeling 18-pulse symmetrical ATRUs. The remaining of this paper is organized as follows. Section II briefs the topology of studied DS-ATRU. Section III gives details of development of proposed model. The validation of the model is validated using experiment and simulation in Section IV. The efficiency of the developed model is demonstrated by comparing with behavioral models in Section V. Section VI concludes the paper.

II. Principle of Operation

A schematic diagram of an 18-pulse DS ATRU is shown in Fig. 2. Three sets of voltages are produced by an autotransformer and fed to three diode bridges. The dc outputs of diode bridges are connected in parallel without an IPR. The coil configuration of the phase shifting autotransformer is shown Fig. 3(a). The winding representation on a three-limb core is shown in Fig. 3(b). Each phase has eight windings and is marked as $1x$, $2x, \ldots$ $8x$ $(x = a, b, c)$. The autotransformer has its primary winding connected in delta configuration across the main supplies v_a, v_b, and v_c. The secondary windings are used to generate

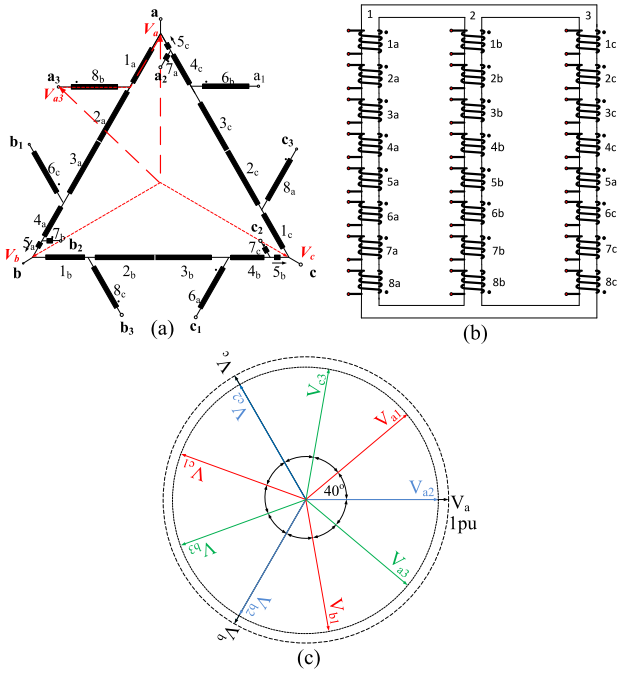

Fig. 3. (a) Configuration of an autotransformer; (b) windings on a three-limb core; and (c) voltage phasor diagram.

required three voltage sets (v_{a1}, v_{b1}, v_{c1}), (v_{a2}, v_{b2}, v_{c2}), and (v_{a3}, v_{b3}, v_{c3}). On the secondary side, the phase shift between adjacent voltages is equal to 40° and the magnitude of secondary voltages is 91.3% of the original primary voltage, as shown in Fig. 3(c).

In a transformer, it is well known that the primary and secondary circuits are strongly coupled magnetically. The voltage phasors on the secondary side can be derived by appropriately adding up primary phasors [V_a, V_b, and V_c marked in Fig. 3(a)]. For example, phasor V_{a3} is equal to $V_a + V_{1a} + V_{8b}$. Phasor V_{1a} is developed in the phase *A* winding, which is supplied with a voltage $(V_b - V_a)$. Similarly, V_{8b} is developed in the phase *B* winding, which is supplied with a voltage and $(V_b - V_c)$. The application of trigonometry can be used to determine the winding length in the transformer, as will be shown in Section III-A.

In this paper, the secondary side of the autotransformer is viewed as three channels. Each channel includes one diode bridge supplied by one set of voltage sources from the autotransformer. It is also worth noting that, with the selected

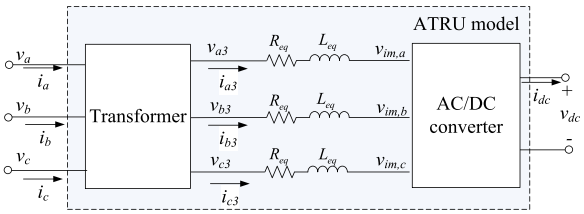

Fig. 4. Equivalent representation of 18-pulse ATRU.

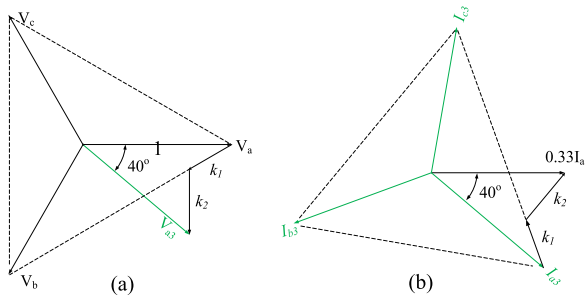

Fig. 5. Voltage and current phasor diagram of autotransformer. (a) Voltage phasor diagram and (b) current phasor diagram.

phase-shifting autotransformer, the three diode bridges are equal to a nine-phase ac/dc converter. The design of this autotransformer is presented in [6] and [19]. Since we are focusing on modeling of autotransformers, the design process will not be detailed in this paper. Instead, the parameters and length of each winding are given in the Appendix.

III. Functional Model of 18-Pulse ATRUs

In this section, the development of a functional model for the DS 18-pulse ATRU will be detailed. The aim is to develop a model that represents the voltage and current relations between the primary of the autotransformer (v_a, v_b, v_c), (i_a, i_b, i_c), and the dc terminal of ATRU ($v_{\rm dc}$, $i_{\rm dc}$).

Fig. 3(a) reveals that the voltage phasor V_{a3} on the secondary side can be represented using phasors V_a, V_b, and V_c. The same procedure can be applied to the current phasors. Moreover, considering the fact that the ATRU dc side voltage and current are strongly related to its ac terminal variables at the diode bridges, i.e., the secondary side of the autotransformer, the original 3–9-dc ATRU system might be simplified into a 3–3-DC system. As shown in Fig. 4, the original 18-pulse ATRU is reduced into three parts: an ideal transformer, equivalent *RL* circuits and a rectifier. The ideal transformer represents the autotransformer using the primary supply and one channel at the secondary side, i.e., reducing the 3–9 phase transformer to a 3–3 phase transformer. The rectifier part embodies the relations between the selected secondary windings and dc terminals of ATRU. The coil resistance and leakage inductance of the transformer are represented by R_{eq} and L_{eq} respectively. The development of the DQ0 model for the 18-pulse ATRU thus involves three steps:

1) Reducing the system order. This step can be achieved: using the character of the autotransformer, i.e., voltage and current relations between primary and secondary sides. The 3–9-dc system in Fig. 2 can be reduced and simplified into a 3–3-dc system as shown in Fig. 4.
2) Transforming the simplified system into the *dq* frame. This step is essentially using the space vector concept, i.e., developing relations between ATRU input voltage vector $\overrightarrow{v}$ of (v_a, v_b, v_c) and the rectified voltage $v_{\rm dc}$; similarly, the current vector $\overrightarrow{i}$ of (i_a, i_b, i_c) and the rectified current $i_{\rm dc}$.
3) Defining the equivalent leakage inductance and resistance.

A. Ideal Transformer

This section aims to develop the voltage and current relations between the primary side and a selected channel, channel No. 3 in this paper, at the secondary side of the autotransformer. Since the selected channel is strongly connected with both the primary side of the autotransformer and the dc-link side, it functions as a key element to reduce the 3–9-DC ATRU system to a 3–3-DC system. In the ATRU shown in Fig. 2, the ac power transferred from the primary side is shared between three channels on the secondary side, carrying (i_{a1},i_{b1},i_{c1}), (i_{a2},i_{b2},i_{c2}), and (i_{a3},i_{b3},i_{c3}), respectively. The magnetic coupling of primary and secondary coils makes it possible to establish relations between primary side and one channel on the secondary side. The channel 3 that carries (i_{a3},i_{b3},i_{c3}) is selected and the relationship between variables in the primary windings and secondary windings is derived as detailed later.

The relationship between voltage sets (v_a, v_b, v_c) and (v_{a3}, v_{b3}, v_{c3}) can be derived according to the phasor diagram in Fig. 5(a) as

$$\begin{cases} v_{a3} = v_a + \dfrac{k_1}{\sqrt{3}}(v_b - v_a) + \dfrac{k_2}{\sqrt{3}}(v_b - v_c) \\ v_{b3} = v_b + \dfrac{k_1}{\sqrt{3}}(v_c - v_b) + \dfrac{k_2}{\sqrt{3}}(v_c - v_a) \\ v_{c3} = v_c + \dfrac{k_1}{\sqrt{3}}(v_a - v_c) + \dfrac{k_2}{\sqrt{3}}(v_a - v_b) \end{cases} \tag{1}$$

where $k_1 = 0.347$ and $k_2 = 0.413$ are the turn ratio between primary and secondary windings of the transformer. Writing (1) in a matrix form yields

$$\begin{bmatrix} v_{a3} \\ v_{b3} \\ v_{c3} \end{bmatrix} = \begin{bmatrix} 1 - \dfrac{k_1}{\sqrt{3}} & \dfrac{k_1}{\sqrt{3}} + \dfrac{k_2}{\sqrt{3}} & -\dfrac{k_2}{\sqrt{3}} \\ -\dfrac{k_2}{\sqrt{3}} & 1 - \dfrac{k_1}{\sqrt{3}} & \dfrac{k_1}{\sqrt{3}} + \dfrac{k_2}{\sqrt{3}} \\ \dfrac{k_1}{\sqrt{3}} + \dfrac{k_2}{\sqrt{3}} & -\dfrac{k_2}{\sqrt{3}} & 1 - \dfrac{k_1}{\sqrt{3}} \end{bmatrix} \begin{bmatrix} v_a \\ v_b \\ v_c \end{bmatrix}. \tag{2}$$

It is important to notice that the (2) is exclusively dependent on the transformer configuration and is not affected by the operational condition of the transformer, i.e., under both balanced and unbalanced power supplies. Defining following vectors:

$$\vec{v} = \frac{2}{3}\left(v_a + v_b e^{j2\pi/3} + v_c e^{j4\pi/3}\right) \tag{3}$$

$$\vec{v}_3 = \frac{2}{3}\left(v_{a3} + v_{b3}e^{j2\pi/3} + v_{c3}e^{j4\pi/3}\right) \tag{4}$$

we can derive the relation of vector magnitudes of $\overrightarrow{v}_3$ and $\overrightarrow{v}$ as

$$\|\vec{v}_3\| = 0.913\,\|\vec{v}\|\,. \tag{5}$$

Since there is no provision of energy storage as current is transferred through ideal transformers, the instant power at the primary side should be equal to that of the secondary side, i.e.,

$$\sum_{j=a,b,c} v_j i_j = \sum_{n=1,2,3}\sum_{m=a,b,c} v_{mn} i_{mn}. \tag{6}$$

Writing (6) in a matrix form yields

$$\begin{bmatrix} i_a \\ i_b \\ i_c \end{bmatrix}^T \begin{bmatrix} v_a \\ v_b \\ v_c \end{bmatrix} = \begin{bmatrix} i_{a1} \\ i_{b1} \\ i_{c1} \end{bmatrix}^T \begin{bmatrix} v_{a1} \\ v_{b1} \\ v_{c1} \end{bmatrix} + \begin{bmatrix} i_{a2} \\ i_{b2} \\ i_{c2} \end{bmatrix}^T \begin{bmatrix} v_{a2} \\ v_{b2} \\ v_{c2} \end{bmatrix} + \begin{bmatrix} i_{a3} \\ i_{b3} \\ i_{c3} \end{bmatrix}^T \begin{bmatrix} v_{a3} \\ v_{b3} \\ v_{c3} \end{bmatrix}. \tag{7}$$

Assuming all the power is transferred from channel No. 3 derives

$$\begin{bmatrix} i_a \\ i_b \\ i_c \end{bmatrix}^T \begin{bmatrix} v_a \\ v_b \\ v_c \end{bmatrix} = K_{p1} \begin{bmatrix} i_{a3} \\ i_{b3} \\ i_{c3} \end{bmatrix}^T \begin{bmatrix} v_{a3} \\ v_{b3} \\ v_{c3} \end{bmatrix} \tag{8}$$

where K_{p1} is a coefficient making sure the power is balanced and it is exclusively dependant on the configuration of the autotransformer. Equation (8) implies the power transferred through the third channel is proportional to the total power. Under balanced conditions, it is obvious that $K_{p1} = 3$. This is due to the fact that the three channels are sharing the power equally at the secondary side of the transformer under balanced conditions. For other types of ATRUs, the power is not necessarily equally shared in the three channels under balanced conditions and the coefficient K_{p1} needs to be calculated to ensure the power balance of the model. This will be explained later.

Substituting (2) into (8) yields

$$\begin{bmatrix} i_a \\ i_b \\ i_c \end{bmatrix} = \mathrm{K_{p1}} \begin{bmatrix} 1 - \frac{k_1}{\sqrt{3}} & -\frac{k_2}{\sqrt{3}} & \frac{k_1}{\sqrt{3}} + \frac{k_2}{\sqrt{3}} \\ \frac{k_1}{\sqrt{3}} + \frac{k_2}{\sqrt{3}} & 1 - \frac{k_1}{\sqrt{3}} & -\frac{k_2}{\sqrt{3}} \\ -\frac{k_2}{\sqrt{3}} & \frac{k_1}{\sqrt{3}} + \frac{k_2}{\sqrt{3}} & 1 - \frac{k_1}{\sqrt{3}} \end{bmatrix} \begin{bmatrix} i_{a3} \\ i_{b3} \\ i_{c3} \end{bmatrix}. \tag{9}$$

As can be noticed, the matrix in (9) is actually the transpose of that in (2). Based on (9), a current phasor diagram can be drawn and is shown in Fig. 5(b). The same diagram can be drawn using other secondary winding variables. It is crucial to notice that the diagram shown in Fig. 5 is exclusively dependant on the autotransformer configuration. Equation (9) can also be derived from Magneto-Motive Force equations of each limb core in the transformer as used in [20], where the authors derived current relations for a 12-pulse ATRU.

Defining the current vector as that in (3) and (4), we can derive following relations from (9) as follows:

$$\left\|\vec{i}\right\| = 0.913\mathrm{K_{p1}}\left\|\vec{i}_3\right\|. \tag{10}$$

The vectors defined as those in (3) and (4) can be expressed in a synchronously rotating frame, i.e., *dq* frame. The *d*- and *q*-axes components can be calculated using the following equation:

$$f_{dq0} = K_s f_{abc} \tag{11}$$

where f_{dq0} represents components in the *dq* frame; f_{abc} are the variables in the three-phase coordinate. The variables in the *dq* frame can also be transformed back to the three-phase coordinate with

$$f_{abc} = K_s^{-1} f_{dq0}. \tag{12}$$

The transformation matrix K_s is written as follows:

$$K_s = \frac{2}{3}\begin{bmatrix} \cos\theta & \cos(\theta - 2/3\pi) & \cos(\theta + 2/3\pi) \\ -\sin\theta & -\sin(\theta - 2/3\pi) & -\sin(\theta + 2/3\pi) \\ 1/2 & 1/2 & 1/2 \end{bmatrix} \tag{13}$$

where θ is the synchronous angle and $\theta = \int \omega dt$. Combining (2), (9), and (11) yields

$$\begin{bmatrix} v_{d3} \\ v_{q3} \\ v_{03} \end{bmatrix} = \begin{bmatrix} 1 - \sqrt{3}k_1/2 & 0.5k_1 + k_2 & 0 \\ -(0.5k_1 + k_2) & 1 - \sqrt{3}k_1/2_1 & 0 \\ 0 & 0 & 1 \end{bmatrix} \begin{bmatrix} v_d \\ v_q \\ v_0 \end{bmatrix} \tag{14}$$

$$\begin{bmatrix} i_d \\ i_q \\ i_0 \end{bmatrix} = \mathrm{K_{p1}} \begin{bmatrix} 1 - \sqrt{3}k_1/2 & -(0.5k_1 + k_2) & 0 \\ 0.5k_1 + k_2 & 1 - \sqrt{3}k_1/2_1 & 0 \\ 0 & 0 & 1 \end{bmatrix} \begin{bmatrix} i_{d3} \\ i_{q3} \\ i_{03} \end{bmatrix}. \tag{15}$$

B. AC–DC Converter

In this section, the voltage and current relations between ac and dc terminals of the ac–dc converter will be detailed.

1) Voltage Relation: In the six-pulse diode bridge, the commutation voltage drop can be represented by an equivalent resistor located on the dc side [21]. The same idea is used for the modeling of the 18-pulse ATRU. The commutation effect associated with the leakage inductance is represented by a resistor at the dc side r_u and the diode bridge itself, thus, is treated as an ideal device.

The relationship between the ac and dc side voltages of the rectifier can be derived as follows:

$$v_{\mathrm{dc}} = \frac{9}{\pi}\int_{-\pi/9}^{\pi/9} \hat{V}_{im}\cos(\omega t)d(\omega t) = \frac{18}{\pi}\hat{V}_{im}\sin\left(\frac{\pi}{9}\right) \tag{16}$$

where v_{dc} is the average dc-link voltage; $\widehat{V}_{im}$ is the maximum value of v_{im} shown in Fig. 4 and it is equal to the magnitude of

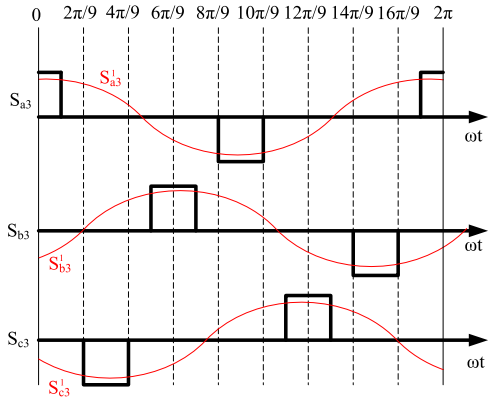

Fig. 6. Switching function of the diode bridge on channel 3 of the ATRU.

vector $\overrightarrow{v}_{im}$ as

$$\vec{v}_{im} = \frac{2}{3}\left(v_{im,a} + v_{im,b}e^{j2\pi/3} + v_{im,c}e^{j4\pi/3}\right). \tag{17}$$

The magnitude of the voltage vector $\overrightarrow{v}_{im}$ can be calculated using

$$\|\vec{v}_{im}\| = \hat{V}_{im} = \sqrt{v_{im,d}^2 + v_{im,q}^2} \tag{18}$$

where $v_{im,d}$ and $v_{im,q}$ are the d- and q-axes components of vector $\overrightarrow{v}_{im}$, respectively. Under balanced conditions, these two variables will be dc-like and $\hat{V}_{im}$ is a constant variable. Under unbalanced conditions, a second harmonic will appear in these two components and $\hat{V}_{im}$ is time dependant. Substituting (18) into (16) gives

$$v_{\rm dc} = \frac{18}{\pi}\sin\left(\frac{\pi}{9}\right)\sqrt{v_{im,d}^2 + v_{im,q}^2}. \tag{19}$$

2) Commutation Loss: The analysis of commutation loss for an 18-pulse rectifier can start from the study of a six-pulse rectifier. For a six-pulse diode bridge, the commutation occurs every $\pi/3$ period and the voltage drop ΔV_d due to commutation is

$$\Delta V_d = \frac{3}{\pi}\omega L_s i_{\rm dc} \tag{20}$$

where L_s is the inductance on the front end of the diode rectifier and $i_{\rm dc}$ is the dc-link current. Similarly, for the 18-pulse rectifier, since the commutation occurs every $\pi/9$, the voltage drop due to that can be expressed as follows:

$$\Delta V_d = \frac{\omega L_s i_{\rm dc}}{\pi/9} = \frac{9}{\pi}\omega L_s i_{\rm dc}. \tag{21}$$

Combining (19) and (21), the dc-link voltage can be written as follows:

$$v_{\rm dc} = \frac{18}{\pi}\sin\left(\frac{\pi}{9}\right)\sqrt{v_{im,d}^2 + v_{im,q}^2} - \frac{9}{\pi}\omega L_s i_{\rm dc}. \tag{22}$$

3) Current Relation: For each diode in the three sets of rectifiers, within the 18-pulse ATRU, the conducting period is $2\pi/9$. The switching functions S_{a3}, S_{b3}, and S_{c3} are shown in Fig. 6 and written as follows:

$$s_{a3} = \frac{4\sin(\pi/9)}{\pi}\sum_{n=1}^{\infty}\cos(n\omega t)\left|\sin\left(\frac{n\pi}{2}\right)\right| \tag{23}$$

$$s_{b3} = \frac{4\sin(\pi/9)}{\pi}\sum_{n=0}^{\infty}\cos(n\omega t - 2n\pi/3)\left|\sin\left(\frac{n\pi}{2}\right)\right| \tag{24}$$

$$s_{c3} = \frac{4\sin(\pi/9)}{\pi}\sum_{n=0}^{\infty}\cos(n\omega t + 2n\pi/3)\left|\sin\left(\frac{n\pi}{2}\right)\right|. \tag{25}$$

Since the model is developed at the functional level, the higher harmonics arising from the switching functions are neglected and only their fundamentals S_{a3}^1, S_{b3}^1, and S_{a3}^1 are considered as shown in Fig. 6. The relationship between the currents at the ac terminals and the dc terminals of the rectifier is

$$[i_{a3}, i_{b3}, i_{c3}]^T = \left[S_{a3}^1, S_{b3}^1, S_{c3}^1\right]^T i_{\rm dc}. \tag{26}$$

Substituting (23)–(25) to the (26) and using the ABC/DQ0 transformation (12) yields

$$\left\|\vec{i}_3\right\| = \frac{4\sin(\pi/9)}{\pi} i_{\rm dc} \tag{27}$$

where $\left\|\vec{i}_3\right\|$ is the magnitude of the current vector for current set (i_{a3}, i_{b3}, i_{c3}) and is calculated as follows:

$$\left\|\vec{i}_3\right\| = \sqrt{i_{3,d}^2 + i_{3,q}^2}. \tag{28}$$

Neglecting the internal inductance, the snubber resistance and capacitance of diodes and considering no storage for diode bridges, the fundamental components of voltage and current on the ac side are in phase. Thus, the phase angle of the ac current vector can be given from the voltage vector

$$\theta_{i3} = \tan^{-1}(v_{im,q}/v_{im,d}). \tag{29}$$

Hence, the currents on the d- and q-axes are

$$i_{3,d} = \left\|\vec{i}_3\right\|\cos(\theta_{i3}) \tag{30}$$

$$i_{3,q} = \left\|\vec{i}_3\right\|\sin(\theta_{i3}). \tag{31}$$

Equations (27)–(31) give the relationship between the currents on the ac and dc sides of the ac/dc converter.

C. L_{eq} and R_{eq}

The parameters L_{eq} and R_{eq} can be calculated as below:

$$L_{eq} = L_s + \frac{L_p}{N^2} \tag{32}$$

$$R_{eq} = R_s + \frac{R_p}{N^2} \tag{33}$$

where L_p and L_s are the primary and secondary leakage inductances, respectively, R_p and R_s are the primary and secondary winding resistances, respectively, and N is the turns ratio between the primary and secondary windings.

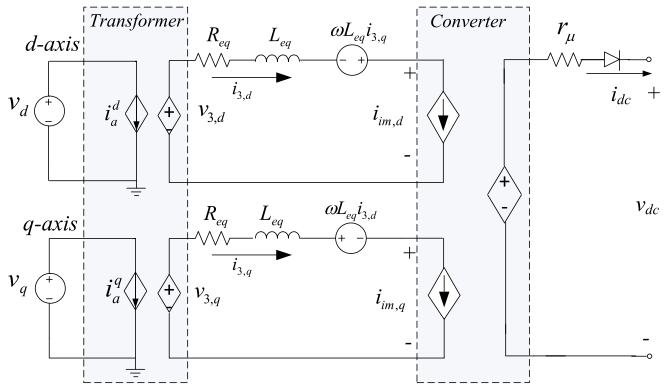

Fig. 7. 18-pulse ATRU model in *dq* frame.

D. Calculation of K_{p1} in General Cases

As mentioned before, under balanced conditions for this type of ATRU, the coefficient $K_{p1} = 3$. However, in general cases (for asymmetric ATRUs, for example), the ac power is not necessarily shared equally in the three channels. The coefficient K_{p1} can be derived assuming a power balance between the ac and dc side of ATRUs. The power on the dc side is calculated as follows:

$$P_{\rm dc} = v_{\rm dc} i_{\rm dc}. \tag{34}$$

Neglecting the leakage inductance and resistance and substituting (5) and (19) into (34) gives

$$\begin{aligned} P_{\rm dc} &= \frac{\sin(\pi/9)}{\pi/18} \hat{V}_{im}\, i_{\rm dc} = \frac{\sin(\pi/9)}{\pi/18} \left\|\vec{v}_3\right\| i_{\rm dc} \\ &= 0.913 \frac{\sin(\pi/9)}{\pi/18} \left\|\vec{v}\right\| i_{\rm dc}. \end{aligned} \tag{35}$$

There is no provision for energy storage (ideally no power loss) as current is transferred through any transformer. Thus, the fundamental component of current at the input must be in the same phase with respect to the input voltage as the output current is with respect to the output voltage [6]. The power at the ac side is expressed as

$$P_{\rm ac} = \frac{3}{2} \left\|\vec{v}\right\| \left\|\vec{i}\right\|. \tag{36}$$

Substituting (10), (27), into (36) yields

$$P_{\rm ac} = 0.913\ {\rm K_{p1}} \frac{3}{2} \frac{4\sin(\pi/9)}{\pi} \left\|\vec{v}\right\| i_{\rm dc}. \tag{37}$$

With power balance $P_{\rm dc} = P_{\rm ac}$, we conclude that

$$K_{p1} = 3. \tag{38}$$

The summary of this section comes to an equivalent DQ0 model of the symmetric 18-pulse ATRU as shown in Fig. 7. The transformer and converter parts are represented as controlled current and voltage sources. This model can be conveniently interfaced with other models developed in *dq* frame, such as synchronous machine [10], etc.

E. Unbalanced Conditions

The unbalanced power supply can be decomposed into positive and negative sequences. Since there is no route for the zero sequence to circulate in the ATRU system, it can be neglected in the analysis. Under unbalanced conditions, (2) can be written as

$$\begin{bmatrix} v_{a3} \\ v_{b3} \\ v_{c3} \end{bmatrix} = \begin{bmatrix} 1-\frac{k_1}{\sqrt{3}} & \frac{k_1}{\sqrt{3}}+\frac{k_2}{\sqrt{3}} & -\frac{k_2}{\sqrt{3}} \\ -\frac{k_2}{\sqrt{3}} & 1-\frac{k_1}{\sqrt{3}} & \frac{k_1}{\sqrt{3}}+\frac{k_2}{\sqrt{3}} \\ \frac{k_1}{\sqrt{3}}+\frac{k_2}{\sqrt{3}} & -\frac{k_2}{\sqrt{3}} & 1-\frac{k_1}{\sqrt{3}} \end{bmatrix} \times \left\{ \begin{bmatrix} v_{a+} \\ v_{b+} \\ v_{c+} \end{bmatrix} + \begin{bmatrix} v_{a-} \\ v_{b-} \\ v_{c-} \end{bmatrix} \right\}. \tag{39}$$

Neglecting the saturation of the autotransformer, it behaves as a linear device. The current relation in (9) can be rewritten in the same way as

$$\begin{bmatrix} i_a \\ i_b \\ i_c \end{bmatrix} = {\rm K_{p1}} \begin{bmatrix} 1-\frac{k_1}{\sqrt{3}} & -\frac{k_2}{\sqrt{3}} & \frac{k_1}{\sqrt{3}}+\frac{k_2}{\sqrt{3}} \\ \frac{k_1}{\sqrt{3}}+\frac{k_2}{\sqrt{3}} & 1-\frac{k_1}{\sqrt{3}} & -\frac{k_2}{\sqrt{3}} \\ -\frac{k_2}{\sqrt{3}} & \frac{k_1}{\sqrt{3}}+\frac{k_2}{\sqrt{3}} & 1-\frac{k_1}{\sqrt{3}} \end{bmatrix} \times \left\{ \begin{bmatrix} i_{a3}^+ \\ i_{b3}^+ \\ i_{b3}^+ \end{bmatrix} + \begin{bmatrix} i_{a3}^- \\ i_{b3}^- \\ i_{b3}^- \end{bmatrix} \right\}. \tag{40}$$

Transforming (39) and (40) into the *dq* frame with (13), the positive-sequence variables become dc components in *d*- and *q*-axes, denoted as (x_{d0}, x_{q0}). The negative-sequence variables appear as the second harmonics in the *d*- and *q*-axes. Thus the negative-sequence can be viewed as a disturbance in the *dq* model and denoted as (Δx_d, Δx_q). Using the Taylor expansion, (19) can be rewritten as

$$\begin{aligned} v_{\rm dc}^2 &= K(v_d^2 + v_q^2) \\ &= K\left\{v_{d0}^2 + v_{q0}^2 + 2v_{d0}\Delta v_d + 2v_{q0}\Delta v_q + \delta(\Delta v_d^2, \Delta v_q^2)\right\}. \end{aligned} \tag{41}$$

However, substituting $v_d = v_{d0} + \Delta v_d$, $v_q = v_{q0} + \Delta v_q$ directly gives

$$\begin{aligned} v_{\rm dc}^2 &= K(v_d^2 + v_q^2) \\ &= K\left\{v_{d0}^2 + v_{q0}^2 + 2v_{d0}\Delta v_d + 2v_{q0}\Delta v_q + \Delta v_d^2 + \Delta v_q^2\right\}. \end{aligned} \tag{42}$$

Comparing (41) and (42), it can be seen that when using v_d and v_q directly, the error is in the order of $\Delta v_d^2 + \Delta v_q^2$. The

same conclusion can be found in the current relations. Thus, the model detailed in previous sections can also be used for unbalanced case studies with acceptable errors.

Summarizing this section, the developed DQ0 model of a symmetrical ATRU can be presented by Fig. 7. The generalized procedure of developing such a model can be formulated as follows:

1) choose one channel on the secondary side of the transformer;
2) derive voltage and current relations between the primary side and the selected channel on the secondary side in the *dq* frame (ac–ac part in the model), similar to (14) and (15) above;
3) define equivalent leakage inductance and resistance as (32), (33);
4) derive voltage and current relations between the selected secondary side and the dc output of the ATRU, using the vector concept, ac–dc part in the model, similar to (22) and (30), (31) in this paper;
5) build the DQ0 model of the ATRU as given by Fig. 7.

The developed DQ0 model can be interfaced with other models developed in the *dq* frame as in [10], [22], where ideal three-phase sources, synchronous machines, transmission lines, etc., are introduced. A three-phase voltage source will become two dc sources in the *dq*-frame model, as shown Fig. 7. The developed DQ0 model can connect with models developed in the three-phase coordinate frame, by using a three-phase to *dq* frame interface. This can be developed using (11) and (12).

IV. Model Validation

Validation of the developed DQ0 model for the 18-pulse ATRU has been completed through experimental test. The developed model is validated with balanced and unbalanced power supplies. In this test rig, the ATRU is supplied by a Chroma 61612 ac source. The Chroma 61612 allows full control of the magnitude and frequency of each phase voltage. The load of the ATRU is a resistive load bank rated at 100 kW@540 V. The 18-pulse ATRU itself is water cooled and rated at 150 kW. The rated voltage of ATRU is 230 Vrms on the ac side and 540 V on the dc side. The diode characteristics: $G_{\rm on} = 666.61\Omega$, $G_{\rm off} = 10^{-6}\Omega$, and $V_{\rm on} = 2.65$ V.

A. Balanced Conditions

The developed model is validated under balanced conditions. Since the load bank is a fixed resistor, the transient response is studied by change of the ac source. The magnitude stepped from 30 to 115 Vrms at $t = 0.02$ s. The phase *A* current i_a flowing into the primary side of ATRU and dc-link voltage $v_{\rm dc}$ are compared between simulation and experimental results in Fig. 8. As can be seen, the currents i_a derived from DQ0 model represent the fundamental of that in experimental results. Fig. 8 also shows good agreement between simulation and experiment in terms of the average dc voltage during transient and steady states.

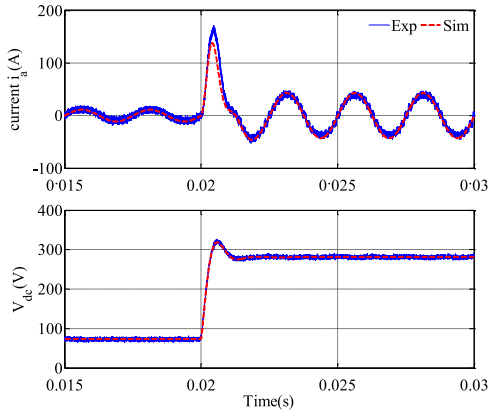

Fig. 8. Comparison between simulation and experimental results, with ac source supply jumps from 30 to 115 V.

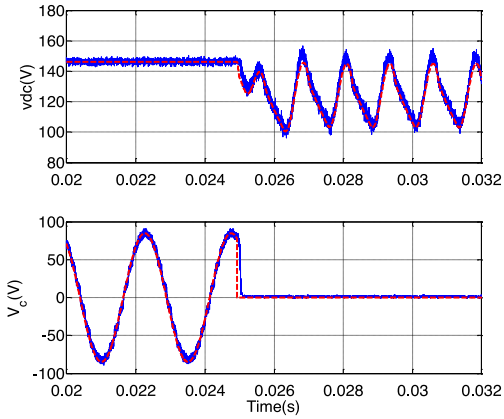

Fig. 9. DC-link voltage and ac power supply v_c of ATRU under balanced and line-to-ground fault conditions.

B. Line-Fault Conditions

The developed model can be used to study unbalanced conditions. In this test, the ATRU is supplied with a balanced AC sources with $\rm Vrms = 60$ V in the beginning. Then, a line-to-ground fault is applied at the primary side of ATRU by setting $v_c = 0$ V, as shown in Fig. 9. The dc-link voltage is also shown in Fig. 9. It can be seen that after fault occurs, the second harmonic (800 Hz) appears in the dc side. This is due to the fact that the magnitude of voltage vector in (17) is not constant and has second harmonic. The currents flowing into the primary side of ATRU are compared in Fig. 10. Since there is no current flowing into phase *C*, i.e., $i_c = 0$ under fault conditions, currents i_a and i_b are opposite, i.e., $i_a = -i_b$. It can be noticed from Fig. 10 that the simulation and experimental results are well matched under both balanced and unbalanced conditions. As one can notice, the model precisely predicts the dc-link voltage under both balanced and faulty conditions.

The line-to-line fault condition test is also studied in this paper. However, due to the current limit of the power source, validations of the model under this condition are carried out through simulations. This will be detailed in the following section.

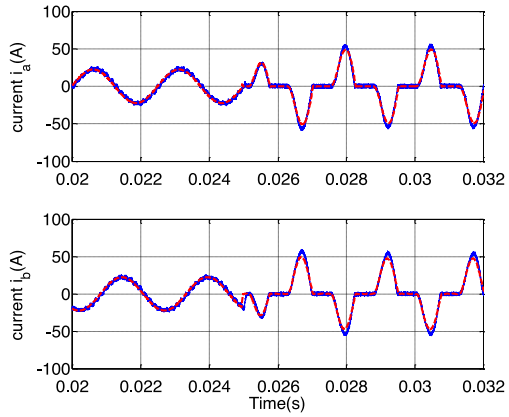

Fig. 10. Phase Current of ATRU under balanced and line-to-ground fault conditions.

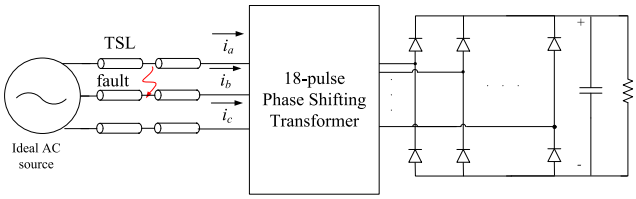

Fig. 11. Simulation scheme of ATUR under line-to-line fault conditions.

V. Simulation Studies

In this section, the efficiency of DQ0 model will be demonstrated. A detailed switching model used as the benchmark is established in Dymola/Modelica and is referred to as ABC model in this paper. The ABC model considers the turning on and off of diodes in the ATRU and the autotransformer is modeled as coupled inductors with leakage inductance and resistance.

The effectiveness of the developed DQ0 functional model of the ATRU is verified by comparison with the ABC model under both balanced and line-to-line fault conditions. The fault is simulated using a short circuit with its resistance $R_{\text{fault}} = 0.1$ mΩ. The resistive load is set at $R_1 = 10\Omega$. Simulations have been performed on an Intel i7 CPU@3.20 GHz, 24.0 GB of RAM using Modelica/Dymola v.7.4 software. The Radau IIa algorithm has been chosen in the solver and the tolerance has been set at 1 e^{-4}. As a quantitative evaluation of the computation efficiency of these modeling techniques, the computation time has been compared. Meanwhile, the evaluation of the accuracy is performed by comparing the plots of the system quantities in figures.

The simulation scheme is shown in Fig. 11 with a line-to-line fault implemented at $t = 0.05$ s between phase *A* and phase *B* at the front end of ATRU. The transmission line is modeled as an *RLC* circuit. Parameters for the system are shown in the Appendix. Fig. 12 shows the phase current flowing into the ac terminals of the ATRU. It can be seen that the DQ0 model and ABC model matched very well under balanced and faulty conditions. Under line-to-line fault conditions, the currents in i_a and i_b are equal. This is due to the fact that phase *A* and phase *B* at the ac terminal of ATRU are short circuited and share the same

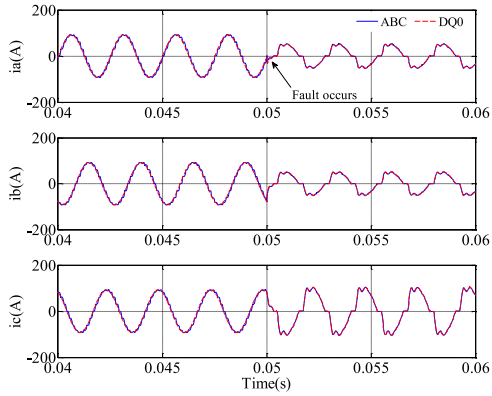

Fig. 12. Comparison of the phase currents flowing into the ATRU between ABC and DQ0 models, with a line-to-line fault occurring at $t = 0.05$ s.

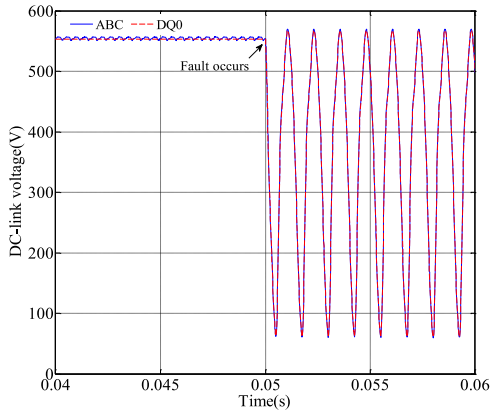

Fig. 13. Comparison of the dc-link voltage between the ABC and DQ0 models, with a line-to-line fault occurring at $t = 0.05$ s.

TABLE I
CPU Time Comparison Between the ABC and DQ0 Models

Scenario	ABC	DQ0	Acceleration
Before fault (0–0.05 s)	72.08	0.12 s	600
Total time (0–0.1 s)	86.52 s	5.081	17

voltage level. Fig. 13 shows the dc-link voltage. Under balanced conditions, the dc-link voltage contains high-order harmonics in the ABC model. The result from DQ0 model in this situation reflects the average value of that in the ABC model. The results from the DQ0 and the ABC models are well matched under both balanced and line-fault conditions.

Table I shows the computation time required by different models during both balanced and unbalanced conditions. It can be seen that before the fault occurs, the DQ0 model is 600 times faster than the ABC model. This is because under balanced conditions, all the variables in the DQ0 model are dc like, which allows the computer using larger simulation steps. However, after the fault occurs, the simulation speed of DQ0 model decreases sharply. This is due to the second harmonics included in the DQ0 model under unbalanced conditions. Table I and Fig. 14 show a comparison of the CPU time required by the two models. Interestingly, it can also identify that simulation of

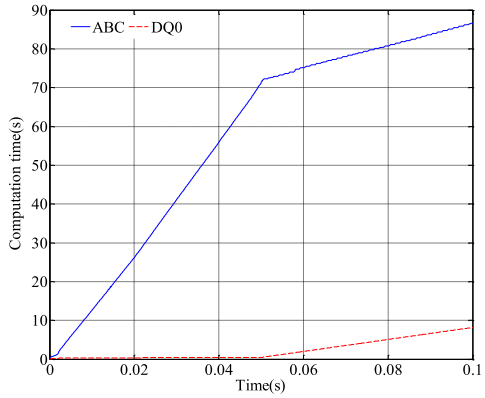

Fig. 14. CPU time comparison between the ABC and DQ0 models, with a step load change at $t = 0.02$ s and a line-to-line fault implemented at $t = 0.05$ s.

ABC model under line-fault conditions is faster than that under balanced conditions. This is due to the fact that under line-fault or unbalanced conditions, the number of conducting diodes in one period is reduced, i.e., less switching behavior in one period.

VI. Conclusion

In this paper, we developed a generic technique in modeling multipulse ATRUs. The proposed technique is introduced and detailed using a direct symmetric 18-pulse ATRU, which will be widely used in the MEA. The DQ0 model developed in this paper has been shown to be highly effective under both balanced and unbalanced conditions. The dynamics of the system are retained well in the developed DQ0 model. The accuracy of developed DQ0 model is demonstrated through experiment under both balanced and line-to-ground faulty conditions. The validation of DQ0 model under line-to-line fault conditions is completed using simulation and compared with ABC model, due to the experiment rig limit. Through simulation, the efficiency of the developed model is also demonstrated. Especially, the DQ0 model is 600 times faster than the ABC model under balanced conditions. The proposed model can also be extended to modeling an asymmetric 18-pulse ATRU. Indeed, the voltage and current vectors at the ac terminals are strongly related to the dc-link voltage and current in the ATRUs. This will be further discussed in future publications.

In addition, the developed model can be easily connected to other functional models developed from previous work. The interface between the DQ0 model and the ABC model can also be conveniently developed using a DQ0/ABC transformation. Under unbalanced conditions, the simulation speed of the DQ0 model decreases sharply, which is due to the double frequency in both *d*- and *q*-axes. The dynamic phasor technique is a potential method that can handle an unbalanced system effectively and a dynamic phasor model for the 18-pulse ATRU in the ABC, and *dq* frames is under development and will be published in future.

Appendix A
The parameters of ATRU experiment are shown below

ATRU parameters: $P_{\text{rate}} = 150$ Kw, $V = 230$ V.

Winding length: $l_{1abc} = 0.347, l_{2abc} = l_{3abc} = 0.512, l_{4abc} = 0.297, l_{5abc} = l_{7abc} = 0.050, l_{6abc} = l_{8abc} = 0.413$.

Connection cable: $R = 0.01\ \Omega$, $L = 2e^{-6}H$, $C = 2e - 9F$.

DC-link side: $C_F = 260\ \mu$F.

Acknowledgment

The authors gratefully acknowledge the EU FP7 funding via the Clean Sky JTI—Systems for green Operations ITD. They would also like to thank Thales for providing the 18-pulse ATRU that was used in our experiment. They also thank Dr. C. Hill for his English correction of this paper.

References

[1] R. E. J. Quigley, "More electric aircraft," in Proc. IEEE 8th Annu. Conf. App. Power Electron. Expo. APEC 1993, pp. 906–911.
[2] A. Uan-Zo-li, R. Burgos, F. Wang, D. Boroyevich, F. Lacaux, and A. Tardy, "Comparison of prospective topologies for aircraft autotransformer-rectifier units," in *Proc. IEEE 29th Annu. Conf. Ind. Electron. Soc.*, 2003, vol. 2, pp. 1122–1127.
[3] K. J. Karimi, "The role of power electronics in more-electric airplanes (MEA)," presented at the Workshop on Computer Power Electronics, NY, USA, 2006.
[4] B. Singh, S. Gairola, B. N. Singh, A. Chandra, and K. Al-Haddad, "Multipulse AC-DC converters for improving power quality: A review," *IEEE Trans. Power Electron.*, vol. 23, no. 1, pp. 260–281, Jan. 2008.
[5] A. Uan-Zo-Li, R. P. Burgos, F. Lacaux, A. Roshan, F. Wang, and D. Boroyevich, "Analysis of new step-up and step-down direct symmetric 18-pulse topologies for aircraft autotransformer-rectifier units," in *Proc. IEEE 36th Power Electron. Spec. Conf.*, 2005, pp. 1142–1148.
[6] D. A. Paice, *Power Electronic Converter Harmonics: Multipulse Methods for Clean Power*, IEEE Ind. Appl. Soc., Eds. Piscataway, NJ, USA: IEEE Press, 1996.
[7] E. K. Matheson, K., "Power quality specification development for more electric airplane architectures," presented at the *SAE*, Pittsburgh, PA, USA, 2002.
[8] G. R. Kamath, D. Benson, and R. Wood, "A novel autotransformer based 18-pulse rectifier circuit," in *Proc. IEEE 17th Annu. Appl. Power Electron. Conf. Expo. APEC*, 2002, vol. 2, pp. 795–801.
[9] I. Moir and A. Seabridge, *Aircraft Systems: Mechanical, Electrical, and Avionics Subsystems Integration*, 3rd ed. New York, NY, USA: Wiley, 2008.
[10] S. V. Bozhko, T. Wu, C. I. Hill, and G. M. Asher, "Accelerated simulation of complex aircraft electrical power system under normal and faulty operational scenarios," in *Proc. IEEE 36th Annu. Conf.Ind. Electron. Soc.*, 2010, pp. 333–338.
[11] H. Liqiu, W. Jiabin, and D. Howe, "State-space average modelling of 6- and 12-pulse diode rectifiers," in *Proc. Eur. Conf. Power Electron. Appl.*, 2007, pp. 1–10.
[12] A. Cross, A. Baghramian, and A. Forsyth, "Approximate, average, dynamic models of uncontrolled rectifiers for aircraft applications," *Power Electron., IET*, vol. 2, no. 4, pp. 398–409, Jul. 2009.
[13] S. Aghighi, A. Baghramian, and R. E. Atani, "Averaged value analysis of 18-Pulse rectifiers for aerospace applications," in *Proc. IEEE Int. Symp. Ind. Electron.*, 2009, pp. 1498–1503.
[14] A. Griffo and W. Jiabin, "State-space average modelling of synchronous generator fed 18-pulse diode rectifier," in *Proc. 13th Eur. Conf. Power Electron. Appl.*, 2009, pp. 1–10.
[15] S. Jian, B. Zhonghui, and K. J. Karimi, "Small-signal modeling of multipulse rectifiers for more-electric aircraft applications," in *Proc. IEEE Power Electron. Spec. Conf.* , 2008, pp. 302–308.
[16] S. Jian, B. Zhonghui, and K. J. Karimi, "Input impedance modeling of multipulse rectifiers by harmonic linearization," *IEEE Trans. Power Electron.*, vol. 24, no. 12, pp. 2812–2820, Dec. 2009.
[17] P. C. Krause and T. A. Asipo, "Analysis and simplified representations of rectifier - inverter reluctance-synchronous motor drives," *IEEE Trans. Power App. Syst.*, vol. PAS-88, no. 6, pp. 962–970, Jun. 1969.
[18] C.-M. Ong, *Dynamic Simulation of Electric Machinery Using Matlab/Simulink*. Englewood Cliffs, NJ, USA: Prentice-Hall, 1997.

[19] R. C. Fernandes, P. da Silva Oliveira, and F. J. M. De Seixas, "A family of autoconnected transformers for 12- and 18-pulse converters generalization for delta and wye topologies," *IEEE Trans. Power Electron.*, vol. 26, no. 7, pp. 2065–2078, Jul. 2011.
[20] C. Sewan, P. N. Enjeti, and I. J. Pitel, "Polyphase transformer arrangements with reduced kVA capacities for harmonic current reduction in rectifier-type utility interface," *IEEE Trans. Power Electron.*, vol. 11, no. 5, pp. 680–690, Sep. 1996.
[21] N. Mohan, T. M. Undeland, and W. P. Robbins, *Power Electronics: Converters, Applications and Design*. New York, NY, USA: Wiley, 2003.
[22] T. Wu, S. V. Bozhko, G. M. Asher, and D. W. P. Thomas, "Accelerated functional modeling of aircraft electrical power systems including fault scenarios," in *Proc. IEEE 35th Annu. Conf. Ind. Electron.* , 2009, pp. 2537–2544.

Tao Yang received the Ph.D. degree in electrical engineering from the University of Nottingham, Nottingham, U.K., in 2013.

Since 2013, he has been a Researcher with the Power Electronics, Machines and Control Group at the University of Nottingham. His research interests include aircraft electrical power systems and ac drive control.

Serhiy Bozhko (M'96) received the M.Sc. and Ph.D. degrees, in 1987 and 1994, respectively, in electromechanical systems from the National Technical University of Ukraine, Kyiv city, Ukraine.

Since 2000, he has been with the Power Electronics, Machines and Controls Research Group of the University of Nottingham, Nottingham, U.K. He is currently a Principal Research Fellow leading several EU- and industry-funded projects in the area of aircraft electric power systems, including control and stability issues, power management, as well as advanced modeling and simulations methods.

Greg Asher (M'98–SM'02–F'07) received the Ph.D. degree from Bath University, Bath, U.K., in 1979.

He undertook research into superconducting levitators in UCNW Bangor, Wales, before being appointed as a Lecturer in Control in the PEMC Research Group at the University of Nottingham, Nottingham, U.K., in 1984. He received the Chair in Electrical Drives and Control in 2000, was the Head at the School of Electrical and Electronic Engineering from 2004, and an Associate Dean at the Engineering Faculty from 2008. He has 280 publications. His current research interests include autonomous power system analysis and control, aircraft electrical power systems, ac drive control, and sensorless control.

Dr. Asher has served on the EPE Executive Council and as the Chair for the Power Electronics and Drives Technical Committee for the IEEE Industrial Electronics Society.